Anatase-TiO_2 Nanomaterials: Morphological/Size Dependence of the Crystallization and Phase Behavior Phenomena

Marcos Fernández-García,*,† Xianqin Wang,‡ Carolina Belver,† Jonathan C. Hanson,‡ and José A. Rodriguez*,‡

Instituto de Catálisis y Petroleoquímica, CSIC, C/Marie Curie 2, Cantoblanco, 28049-Madrid, Spain, and Department of Chemistry, Brookhaven National Laboratory, Upton, New York 11973

Received: August 31, 2006; In Final Form: October 3, 2006

Nanoparticulated TiO_2 materials with anatase structure were synthesized by using a microemulsion method. Three different syntheses with varying surfactant-to-water molar ratio (ω) were used to obtain amorphous solid precipitates at room temperature. The structural characteristics of these solid precursors were studied by using X-ray absorption structure (X-ray absorption near-edge structure and extended X-ray absorption fine structure) and Raman spectroscopies, which showed that all lack 3D (tridimensional) order but contain a different degree of 2D-confined connectivity. While heating such solid precursors under dry air, marked differences appeared in the phase behavior; the onset temperature for anatase crystallization increases ca. 150 °C while the ω parameter decreases and only one of the samples shows the anatase-to-rutile transformation below 900 °C. In all cases, the crystallization of the anatase structure does not follow a traditional nucleation and growth mechanism and its analysis using the Avrami formalism gives conclusive evidence of a surface nucleation-dominated process. This appears as a distinctive feature of anatase-TiO_2 nanomaterials, far from the corresponding behavior of microsized or bulk materials. After nucleation, the grain growth of anatase nanoparticles was found to follow the kinetic equation $D^2 - D_0^2 = k_0 \exp(-E_a/RT)$, where the activation energy is a function of several structural properties of the solid materials mainly related to the hydration characteristics of the surface layer. A combined in situ X-ray diffraction/Raman/infrared study aimed to unveil the physical basis of the phase behavior and to interpret key variables allowing control of the crystallization mechanism and morphological properties, particularly primary particle size, in the nanometer regime.

Introduction

Titanium dioxide (TiO_2) is one of the most prominent oxide materials for performing various kinds of industrial applications related to catalysis among which the selective reduction of NOx in stationary sources[1,2] and photocatalysis for pollutant elimination[3] or organic synthesis[4] appear as rather important. Additional applications include its use as a white pigment in paintings,[5] as part of photovoltaic devices[6] and sensors,[7] as a food additive,[8] in cosmetics,[9] and as a potential tool in cancer treatment.[10] The (n-type) semiconductor properties of TiO_2 materials are essential in accomplishing these functions. Experimental approaches to scale down the TiO_2 primary particle size to the nanometer scale are now actively being investigated to improve its current applications in sensor or catalysis fields and to reach more advanced ones such as its use in electrochromic devices.[11] As a general result, the nanostructure induces an increase in surface area by the corresponding decrease in the primary particle size with concomitant potential enhancement of the chemical activity (connected with several structural and electronic size-related effects) and also of the photochemical and photophysical activities by reduction of light scattering.[12] In TiO_2 materials, the so-called "quantum-confinement" or "quantum-size effect" is restricted to very low sizes, below 10 nm, due to their rather low exciton Bohr radii. This would mean that a significant part of the potentially important chemical or physical applications needs to be carefully explored in the range of a few nanometers.[12]

TiO_2 occurs in nature in three different polymorphs, which, in order of abundance, are rutile, anatase, and brookite. Additional synthetic phases are called TiO_2(B),[13] TiO_2(H),[14] and TiO_2(R),[15] while several high-pressure polymorphs have been also reported.[16] Anatase appears to be the most important for new chemical applications as it is a stable polymorph at working temperatures for sizes below ca. 15 nm.[17,18] As a consequence, the majority of TiO_2-based nanoparticulated materials display this specific structure. Controlling size (primary particle size) and size-related physicochemical properties in anatase-TiO_2 materials therefore appears to be a rather important issue from a basic point of view but also with technological-added value.

Control of the nanostructure in oxide materials requires, in the first place, the use of adequate synthetic methods. The sol−gel method is becoming a standard in synthesizing ultrafine powder oxides having high chemical homogeneity.[19] Micellar methods use micelles as microreactors in which oxide or oxide precursors are obtained by reaction between solved cations and a precipitating agent. This method is also utilized to obtain ultrafine powders with significant control of chemical homogeneity and particle size.[20] Here we will take advantage of this latter method and use it to control as much as possible morphological characteristics of anatase-TiO_2 materials. It is also well-known that the presence of ionic species during synthesis plays a significant role in the phase behavior of the oxide; high concentrations of Cl^- typically lead to rutile as a

* Corresponding authors. E-mail: m.fernandez@icp.csic.es; rodrigez@bnl.gov.
† Instituto de Catálisis y Petroleoquímica, CSIC.
‡ Brookhaven National Laboratory.

10.1021/jp065661i CCC: $37.00
Published on Web 11/17/2006

TABLE 1: Water/Titanium Molar (*R*) and Water/Surfactant Molar (ω) Ratios Used during the Microemulsion Synthesis of Ti−O Solids

sample	ω	R
T	18	110
TA	4.5	220
TB	3	220

final product of the synthesis at low temperature,[21] while SO_4^{2-} results in anatase formation.[22] To overcome/minimize the "contamination/impurity" problem, Ti isopropoxide is commonly used as a Ti precursor. Once obtained after the liquid-phase synthesis stage, all oxide precursors are subjected to thermal or hydrothermal treatments.[19,20] Crystallization of oxide phases from amorphous or nearly amorphous grains of chemically pure Ti−O materials is still a fairly unknown process that does not seem to proceed by classic nucleation and growth and that nevertheless has received a lot of attention in recent years.[23−26] Particle growth kinetics and initial growth conditions lead to the formation of single or multiple phases with significant differences in morphological properties and particularly in primary particle size.

In this article, we will seek a fundamental understanding of the crystallization mechanism in the case of nanoparticulated anatase-TiO_2 materials. To reach this objective, we will obtain several Ti−O oxide precursors using a microemulsion method and analyze their relevant electronic and structural properties in their initial state by performing in situ studies of the initial materials and their evolution upon heating in dry air, first to the anatase structure and, when occurring, to the rutile one. Our main aim is to study key variables controlling the formation of the adequate structure (e.g., anatase) and, more importantly, affecting the morphological properties (e.g., primary particle size and shape) in the nanoscale world. Our results show that the crystallization of the anatase nanoparticles does not follow a traditional nucleation and growth mechanism.

Experimental Section

Preparation of the TiO_2 Oxide Precursors. Ti−O precursor materials were prepared using a microemulsion synthetic route by addition of titanium(IV) isopropoxide (Aldrich) to an inverse emulsion containing an aqueous phase (50 mL) dispersed in *n*-heptane (85/10 v/v versus H_2O; Panreac), using Triton X-100 (variable quantity; Aldrich) as surfactant and 1-hexanol (105/100 v/v versus surfactant; Aldrich) as cosurfactant.[27] The resulting mixture was vigorously stirred for 24 h, centrifuged, decanted, rinsed under stirring five consecutive times with methanol (2), water (2), and acetone (1) to eliminate any portion from the organic and surfactant media, and dried at 110 °C for 24 h. Sample labels and main synthesis details are summarized in Table 1.

Characterization Experiments. The Ti K-edge X-ray absorption near-edge structure (XANES) and extended X-ray absorption fine structure (EXAFS) spectra of Ti−O precursor materials were collected at the National Synchrotron Light Source (NSLS) on beam line X19A in the "fluorescence-yield mode" using a double-Si(111) crystal fixed-exit monochromator with feedback on second crystal and a special cell with a modified PIPS detector.[29] All the XANES spectra were taken at room temperature using a constant scan step of 0.5 eV through the edge region, and the energy resolution was close to 0.4−0.7 eV. EXAFS spectra were taken using several regions with a constant *k* step (ca. 0.03 $Å^{-1}$) up to above 13 $Å^{-1}$. A bulk rutile reference was also obtained in fluorescence and transmission mode to correct for self-absorption phenomena. Ti−O/Ti−Ti phase and amplitude functions were extracted from bulk anatase-TiO_2/Ti materials. Fitting results were obtained by using the VIPER program (www.dessy.de/∼klmn/viper.html),[28] and error bars were estimated with k^1/k^3 weighted fittings. The number of free parameters allowed by the fitting *k* (2.95−11.9 $Å^{-1}$) and *R* (0.60−3.06 Å) ranges used is above 20 according to the Nyquist theorem ($N_{free} = 2\Delta k\Delta R/\pi + 1$).

Analysis of solid and gas phases evolved from the precursors under thermal treatment was performed by using a thermogravimetric mass spectrometer (TG-MS) system from Perkin-Elmer TG-7. Samples were treated in dry air at 110 °C and cooled in nitrogen. After the pretreatment, they were subjected to a heating ramp of 10 °C min^{-1} from 25 to 925 °C under a 20% O_2/He. The evolving gaseous products were detected by mass spectrometry; only H_2O ($m/z = 17, 18$), CO ($m/z = 44$), and CO_2 ($m/z = 44$) molecules were observed in the experiments. Differential thermal analysis (DTA) experiments (Perkin-Elmer) were also performed in parallel.

The time-resolved X-ray diffraction data were collected at beamline X7B ($\lambda = 0.9220 \pm 0.0005$ Å) of the NSLS in Brookhaven National Laboratory (BNL). The wavelength calibration was determined with the FIT2D code based on the diffraction pattern for LaB_6.[29,30] In the TR-XRD experiments dealing with the thermal evolution of Ti−O nanomaterials, the sample (ca. 30 mg) was kept in a sapphire capillary and heated using a small resistance heater placed around the capillary from 25 to 925 °C under a 5% O_2/He.[30] A chromel−alumel thermocouple was used to measure the temperature of the sample. Two-dimensional powder patterns were collected with a Mar345 image plate detector, and the powder rings were integrated using the FIT2D code.[31] Average grain and particle domain sizes (*D*) were calculated from the most intense diffraction peak (101) using the Scherrer formula.[32]

Raman spectra were obtained at room temperature with a Renishaw Dispersive System 1000, equipped with a cooled TCD and holographic Notch filter. The samples were excited with the 514-nm Ar line in an in situ cell (Linkam TS-1500), which allowed treatment under controlled atmospheres. Samples of ca. 40 mg were dried in situ at 110 °C with synthetic air (20% O_2 in He) and ramped at 5 °C min^{-1} up to 900 °C. Isothermal experiments for kinetic characterization were carried out at three different temperatures for each sample. The spectra consisted of 50 accumulations with a total of ca. 1 to 2 min acquisition time, using a typical running power of 2−10 mW. Care was taken in minimizing heating of the samples; peak positions were found to be constant within 2 to 3 cm^{-1}.

Diffuse reflectance infrared Fourier transform spectra (DRIFTS) were taken in a Bruker Equinox 55 FTIR spectrometer fitted with an MCT detector. The DRIFTS cell (Harrick) was fitted with CaF_2 windows and a heating cartridge that allowed samples to be heated to 700 °C. Samples of ca. 60 mg were dried in situ at 110 °C with synthetic air (20% O_2 in He) and ramped at 5 °C min^{-1} up to 700 °C. The spectra consisted of 100 accumulations with a total of 2 min acquisition time, using a 4 cm^{-1} resolution.

Results and Discussion

Precursor Materials. The Ti−O precursor materials mainly contain Ti and O components. TG experiments (see below) indicate that all have well below 3 wt % of organic residues. The chemical nature and structural characteristics of these materials were analyzed using X-ray absorption spectroscopies (XAS). In Figure 1A, we display the XANES spectra of the three precursor materials; all show broad and featureless

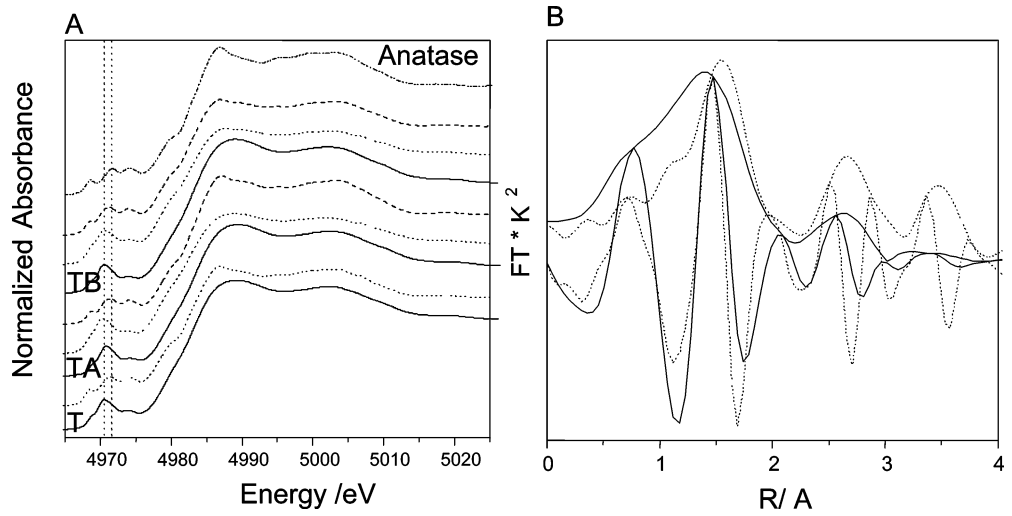

Figure 1. (A) XANES spectra of solids treated at room temperature (full line); 450 °C (dotted line), 600 °C (dashed line), and bulk anatase reference (dash-dotted line). (B) Fourier transform and imaginary part of the EXAFS spectra of the T sample (full line) and a bulk anatase sample (dotted line).

continuum resonances that clearly resemble those characteristic of the anatase-TiO_2 phase appearing after calcination at high temperatures in all samples. The XANES spectra also show pre-edge features ascribable to the dipole 1s → 3d transition; the peak shape shows a prominent contribution at ca. 4970.5 eV, on top of a structure (e.g., three resolved peaks) characteristic of six-coordinated (Ti_{6c}^{4+}) cations located on the anatase-TiO_2 structure. Such Ti_{6c}^{4+} local structure is again better visualized in the samples calcined at high temperature. The 4970.5 eV peak gives evidence for the presence of five (Ti_{5c}^{4+}) coordinated cations.[12,33−35] The XANES analysis therefore shows that the local environment in our Ti−O precursors contains a mixture of Ti_{5c}^{4+}/Ti_{6c}^{4+} cation species within an anatase-type local order.[12,36] To better define the close environment of Ti cations, we also performed an EXAFS study. All precursor samples display, within error, the same signal, and an illustrative result (EXAFS signal Fourier transform of sample T) is presented in Figure 1B together with a bulk anatase-TiO_2 reference system. At first look, the presence of additional neighbors at distances below the Ti−O first shell of bulk anatase and a significant loss of coordination number for neighbors sited at larger distances can be noted. The numerical analysis gives in fact two Ti−O shells at 1.72−175 and 1.90−1.92 Å and a Ti−Ti contribution at 3.02−3.03 Å (phase-corrected distances). For comparison, we can mention that bulk anatase displays six oxygens at ca. 1.95 Å and four Ti at distances around 3.05−3.10 Å, depending of the primary particle size of the material.[12,34] The shorter Ti−O distance is likely associated with the presence of Ti_{5c}^{4+} centers, but for our purposes, the main point is that the Ti−Ti shell located around 3.02 Å has a coordination number of 2.2 ± 0.5. This would mean that the Ti cation has almost a chainlike structure without (or with severely limited) tridimensional (3D) connectivity. The joint XANES and EXAFS analysis would thus indicate that the precursor materials display Ti_{5c}^{4+}/Ti_{6c}^{4+} coordinated cations with a limited connectivity mainly constituted by −Ti−O−Ti− links and local order compatible with a defective-like anatase-type structure. No significant local structural differences are encountered among the samples.

This relative similarity among precursors can be further analyzed using Raman (Figure 2). Raman is sensitive from middle to long range order, allowing to complete and expand information obtained from XAS spectroscopies. Raman spectra taken at room temperature gives similar frequencies at ca. 215, 425, 610−635, 850−870, and 1020 cm^{-1}. A weak shoulder at 1020 cm^{-1} may indicate the presence of carbonyl moieties coming from isopropoxide residues.[37] The first four frequencies, on the other hand, are usually detected in amorphous Ti−O materials[37,38] and ascribed to Ti−O bending (215, 425 cm^{-1}), Ti−O stretching (610−635 cm^{-1}), and Ti−O−Ti stretchings (850−870 cm^{-1}). The latter may also have contributions from a Ti−O stretch assigned to the short Ti−O bonds detected by EXAFS. In any case, the larger intensity of this latter peak in the T sample would in fact indicate a somewhat better 2D-type connectivity. Thus, from a structural point of view, the multi-technique XAS/Raman approach used here provides evidence of the presence of −Ti−O−Ti− chainlike structures with an important shortening of Ti−O (first coordination) distances with respect to the anatase structure. Raman shows a lack of significant 3D order, indicating a limited, 2D-constrained kernel of order around Ti cations (with cation−cation contacts restricted to a 1D chainlike structure at a local level) which seems better developed in the case of the T precursor.

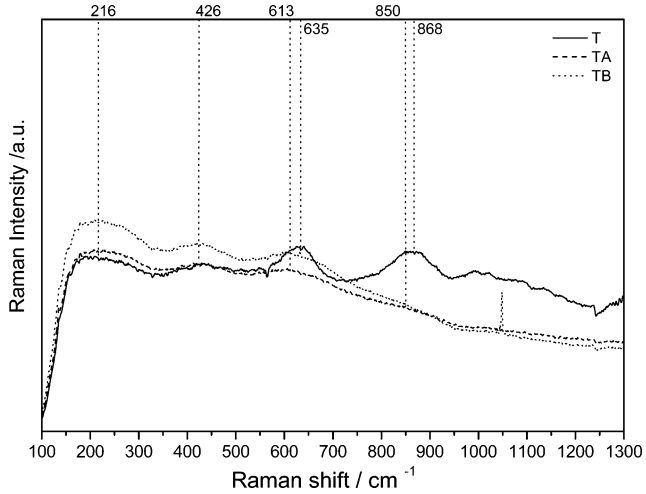

Figure 2. Raman spectra of the Ti−O samples at room temperature.

Genesis of the Anatase Phase. The thermal evolution of the Ti−O nearly amorphous materials under a O_2/He atmosphere was investigated using several techniques. In Figure 3, we present a TG-MS/DTA study. As stated earlier, the TG-MS results provide evidence of the limited weight loss detected, below ca. 7%, in all cases. Mass spectrometry indicates the

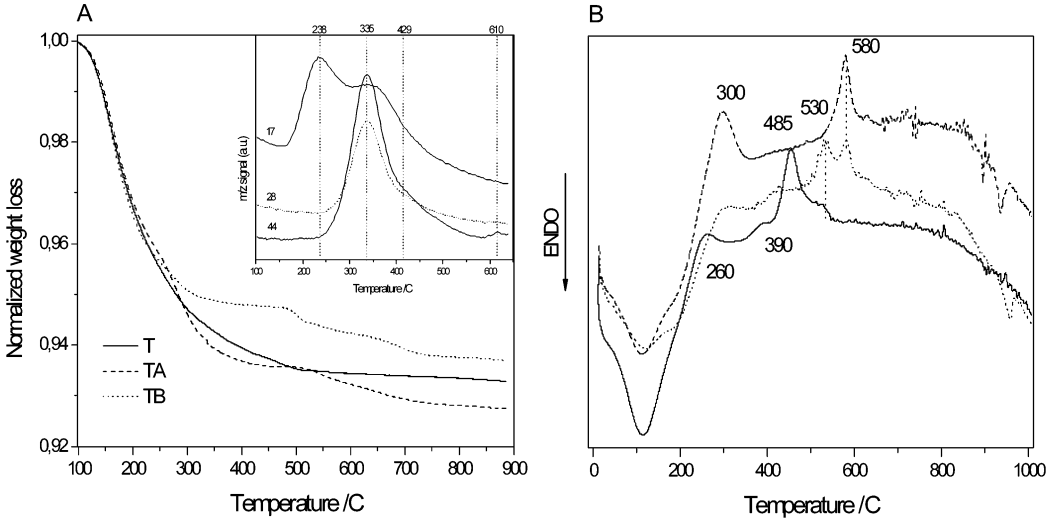

Figure 3. (A) Normalized weight loss of Ti−O samples during thermal treatment in dry air. Inset: TA mass signals of the evolving gas-phase products. (B) DTA profiles of Ti−O samples during thermal treatment in dry air.

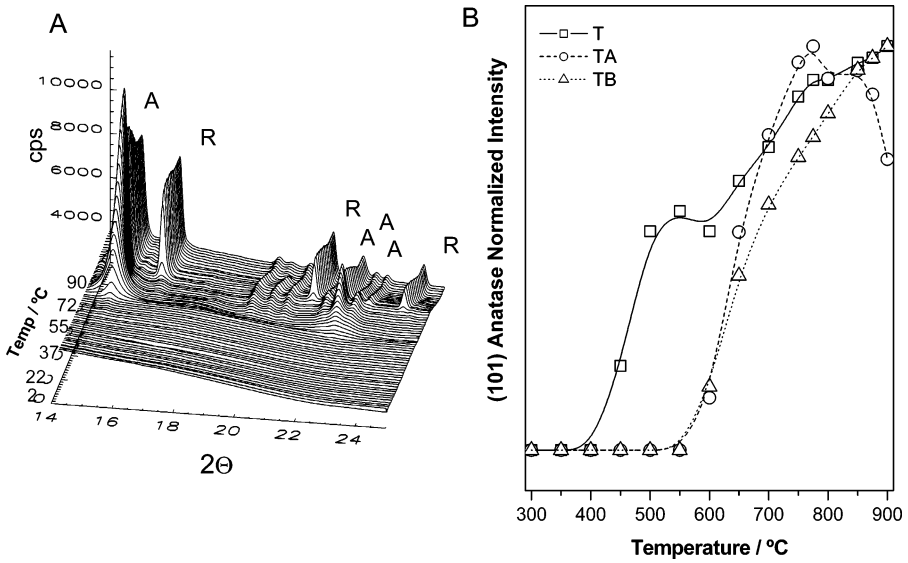

Figure 4. (A) XRD diffractograms of the TA sample during a heating treatment under dry air (A/R labels ascribe peaks to anatase/rutile phases). (B) Normalized intensity of the (101) anatase reflection of Ti−O samples as a function of the temperature of the heating treatment.

exclusive presence of CO_2/CO (as confirmed with the *m*/*z* 12 versus *m*/*z* 28/44 signals parallel behavior) and water (*m*/*z* = 17, 18) as evolving gases from the treatment. Although samples are dried at 110 °C overnight, water is the exclusive gaseous product evolving below 250 °C. Above this temperature, C-containing gases ascribed to the organic fragments burning are detected together with water. The TG plot shows (Figure 3A) that the organic residues only account for 2 to 3 wt % of the initial solid. The parallel DTA experiments (Figure 3B) indicate that these organic fragments are burned mainly in the temperature region between 260 and 350 °C,[39] although small and featureless peaks are also detected up to ca. 450 °C. The anatase crystallization appears to take place at different temperatures in our samples; while the T sample develops such structures below 500 °C, TA and TB samples do it around 50−100 °C after the T material. Differences among samples are further visualized using XANES (Figure 1), XRD (Figure 4), and Raman (Figure 5). Local order during crystallization was followed by XANES taking spectra each 50 °C. Main differences among samples appear in a limited development of the anatase-type local structure with the concomitant disappearance of Ti_{5c}^{4+} sites in TA/TB samples with respect to T for temperatures below 600 °C. As shown in Figures 4 and 5, anatase is the first nanocrystalline phase detected by the presence of the (101) peak at ca. 15° in XRD (JCPDS 21-1272) and the Eg mode at ca. 145 cm^{-1} in Raman.[12] The onset temperature of crystallization is clearly seen in Figure 4B: while the T sample starts around 400 °C, TA and TB do it above 550 °C. Raman would enhance differences between these two last samples, showing that TB may start a little earlier (Figure 5).

It would thus appear that the differences in the 2D-type kernel of structural order present among our Ti−O amorphous precursors influence the onset of the crystallization process, with more ordered systems crystallized first, as a simple argument may predict. The influence of the C-containing impurities present in the samples seems of lesser importance for interpreting the differential behavior as they disappear well below the nucleation onset and, more importantly, their similar chemical nature as measured by infrared (Figure 6; see C−H stretch modes around 2850−2950 cm^{-1}) and quantity (Figure 3A) would minimize any influence in the differences detected among samples. In brief, these results mean that strong differences are encountered in the nucleation transformation onset among our samples and these are mainly dominated by the ω parameter of the micro-

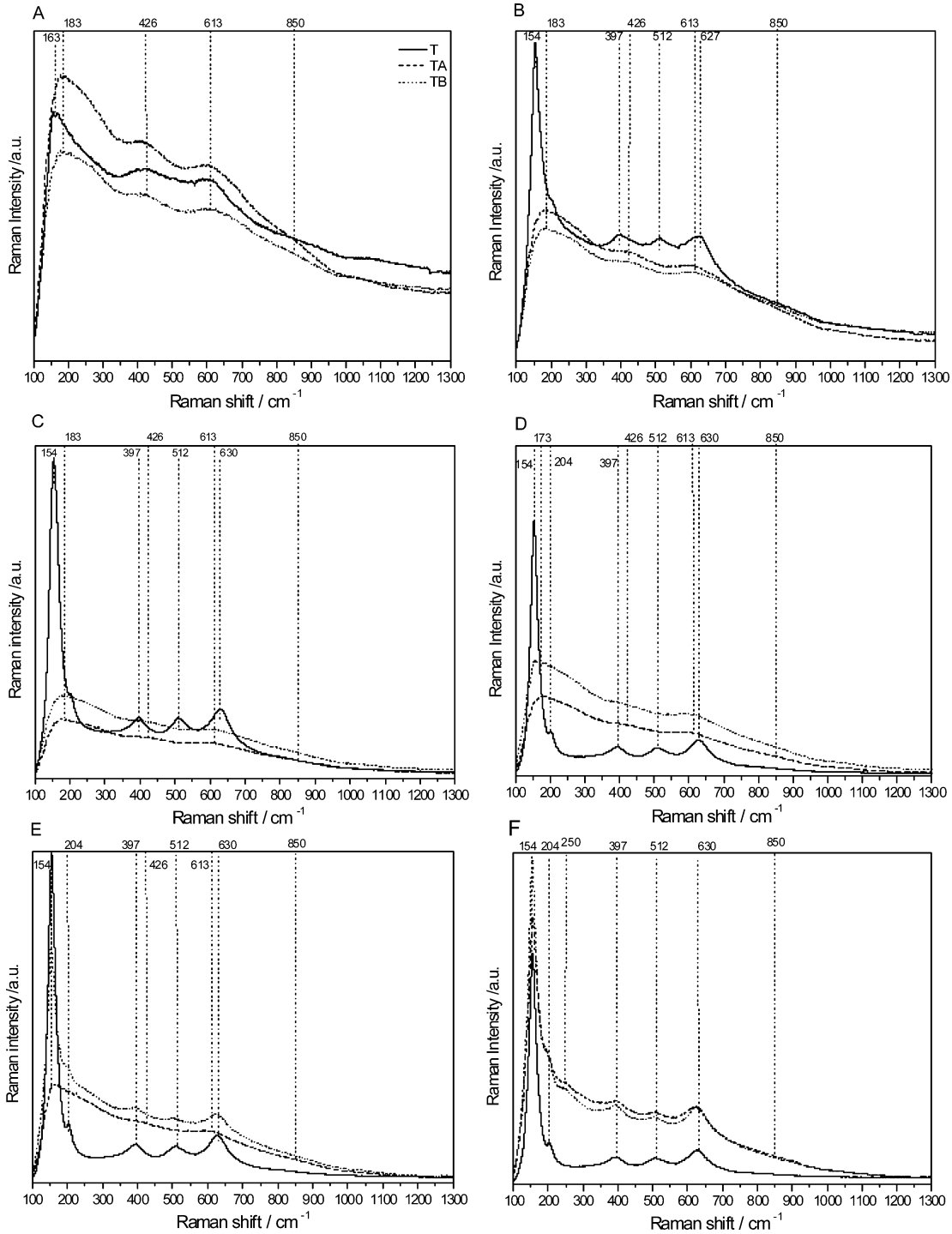

Figure 5. Raman spectra of Ti−O samples at different temperatures: (A) 400, (B) 450, (C) 500, (D) 600, (E) 650, and (F) 700 °C.

emulsion synthesis. Uskokovic and Drofenik[20] were able to show that two well-differentiated situations may occur when such a parameter is above or below ca. 6−10 due to a limited availability of water molecules in the latter case, presumably affecting both the hydrolysis and posterior polymerization and polycondensation of the precursor and the −Ti−O−Ti− links nature and properties present in the resulting solid precursors. The corresponding structural effects produced in these two situations will be analyzed in the next section using infrared and Raman spectroscopies.

Crystallization Mechanism and Size Control on a Nanometer Scale. The anatase crystallization mechanism was investigated in detail by a combination of XRD, Raman, and DRIFTS. While microsized oxides have a well-established crystallization mechanism, following the so-called nucleation and growth scheme, research in recent years has opened a number of questions concerning the growth of nanoparticulated materials.[23−26,40]

Many solid-state phase transitions studied by in situ techniques are often well-described using the integrated form of the Avrami equation.[24,41,42] This leads to a sigmoidal type behavior under isothermal conditions. Isothermal Raman data (Figure 7) were analyzed here according to the Avrami equation:

$$\ln[-\ln(1-\alpha)] = n \ln t + n \ln k \qquad (1)$$

where α is the amount of the transformed material, k is the temperature-dependent rate constant, t is time, and n is a

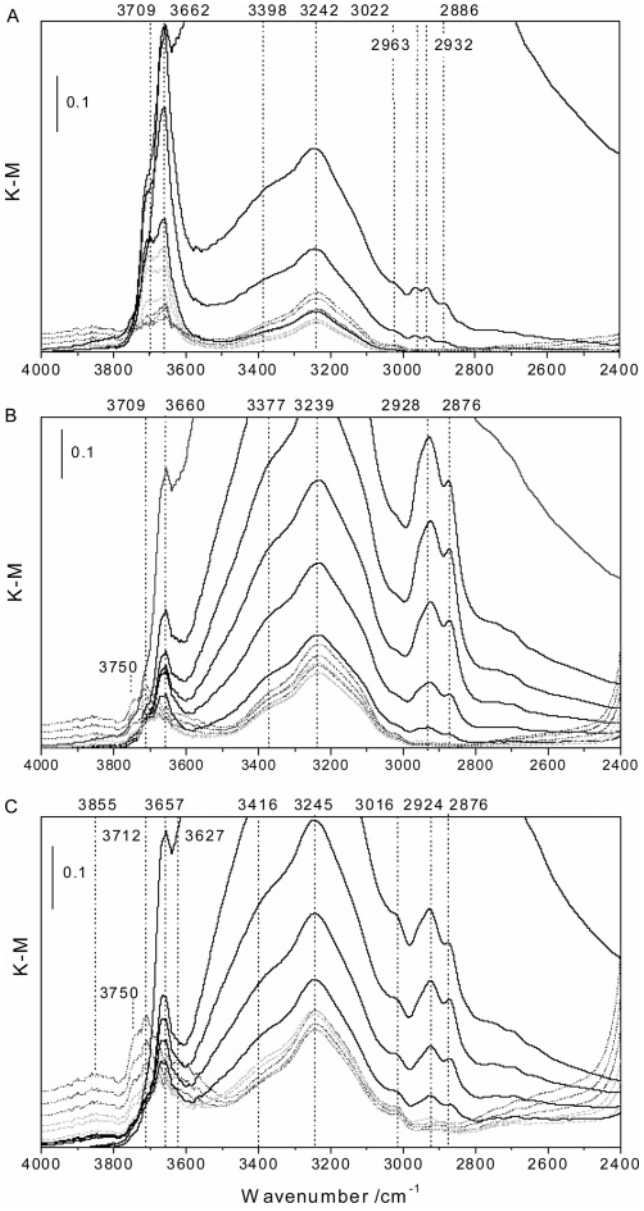

Figure 6. DRIFTS spectra of T (A), TA (B), and TB (C) samples. (A) Spectra recorded at 230, 290, 320, 360, 380, 400, 420, 470, 500, 540, 570, and 595 °C. (B) Spectra recorded at 220, 275, 305, 370, 400, 430, 460, 490, 525, 555, and 585 °C. (C) Spectra recorded at 220, 300, 345, 375, 405, 440, 470, 505, 535, 560, and 590 °C. Gray scale is only included to facilitate spectra differentiation.

parameter that describes how the transformation (e.g., anatase crystallization) propagates through the material. In the derivation of eq 1, *n* contains terms describing both the number of steps involved in nucleation and the number of dimensions in which the nuclei grow. The amount of transformed material is calculated by the intensity of selected Raman peaks associated with the anatase structure. The *n* value is therefore an average, and the information yielded is somewhat limited. In crystallization transformations, nucleation of nanocrystallites may begin in the bulk or at the surface, and as a result the *n* parameter will vary. In nucleation-dominated systems that exhibit surface-nucleated crystallization, the *n* parameter usually has a value of 1. Bulk-nucleated crystallization generally displays *n* parameters larger than 1 and includes both the nucleation and the growth steps of the transformation.[24,41−43]

Values of the *n* parameter are summarized in Table 2. The average *n* values are 1.08, 1.12, and 1.13, respectively, for

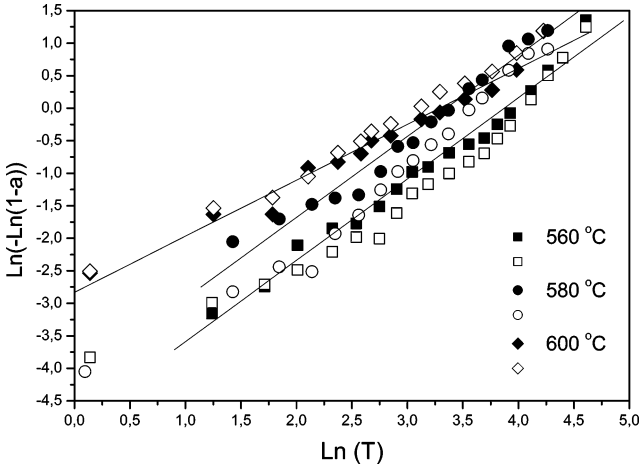

Figure 7. Plots of the Avrami eq 1 to determine the value of the *n*/*k* parameters for TA sample using Raman bands at ca. 145 (full symbols) and 510 (open symbols) cm^{-1}. See text for full details. Linear fittings are presented as solid lines.

TABLE 2: Crystallization and Growth Mechanism Parameters for Ti−O Solids: *n* Parameter of the Avrami Eq 1 and Activation Energies (kJ mol^{-1}) for the Processes Described in Eqs 1 (E_A) and 2 (E_D)

sample	n^a	$E_A{}^b$	$E_D{}^c$
T	1.08	340	14
TA	1.12	160	26
TB	1.13	530	18

[a] Standard error ±0.3. [b] Standard error 30%. [c] Standard error 20%.

samples T, TA, and TB. We have tested the consistency of these values by checking the Raman result with two anatase modes (e.g., bands at ca. 145 and 510 cm^{-1}) and in the case of the T sample using XRD; *n* values are consistent within 0.3 units. Values of *n* reported in Table 2 are equal within error among our three samples and are very close to $n = 1$, thus allowing a surface nucleation-dominated crystallization process to be identified.[44] Anatase crystallization could therefore preferentially nucleate at the surfaces and then essentially be complete almost instantly due to the high surface-to-volume ratio of the nanomaterials. The small amount of grain growth occurring after nucleation can be explained on the basis of the work of Ghost et al.,[23] which showed that a high concentration of dislocations at the grain boundaries is typical of anatase and would severely restrict growth to larger crystallites. The nucleation-dominated crystallization behavior has been observed previously in nanostructured and mesoporous anatase materials and may thus be an inherent property of this nanoparticulated oxide.[24,45] This means that our nanostructured anatase-TiO_2 adopts a crystallization mechanism distant from classic ones followed by the corresponding microsized or bulk oxide.

Because anatase crystallization is a surface-dominated nucleation process, we use DRIFTS to follow sample behavior through changes in surface species during thermal treatments (Figure 6). Recent combined DFT and IR spectroscopy studies have made available and accurate prediction of surfaces morphologies using the latter technique.[46] Here we must recall that such correlations are based on the O−H stretching frequencies of surface-adsorbed groups and that this internal mode only gives structural information at a local level.[47,48] Figure 6A−C presents results for, respectively, our T, TA, and TB precursor materials in the O−H stretch region. While several mutually interacting OH groups, physisorbed water molecules, and C−H stretchings (the latter from organic residues) are observed below 3600 cm^{-1}, OH groups and water molecules giving raise bands above such

a limit allow the desired information to be obtained. Below the nucleation onset temperature, our nearly amorphous systems, displaying only 2D-like order, have OH-containing groups and molecules adsorbed on anatase-type (101)-terminated (3657−3662 cm^{-1}) and (100)-terminated (3709−3712 cm^{-1}) local environments. Additional small contributions at 3750 and 3627 cm^{-1} reflect, respectively, (001)- and (101)-type local terminations in the TA/TB samples.[46−48] While the former (e.g., (101)) is always observed in the Ti−O precursor materials showed in Figure 6, the second (e.g., (100)) is only detected when the temperature rises above 280 °C (T) or 430 °C (TA, TB). Those specific of the TA/TB samples parallel the behavior of the second main band. It thus appears that anatase-type surface terminations are formed well below the nucleation onset and that originally the more stable (101)-, followed by (100)- and, for TA/TB, marginal (001)-type of surfaces appear. A first main difference between samples is that the T material displays a significantly higher number of surface species sited at (100) terminations with respect to TA and TB materials, while the temperature approaches the nucleation onset. It therefore seems that the sample T amorphous precursor has a larger number of (100)-type terminations which may be more stable than those presented in TA and TB specimens at the nucleation onset (see Figure 6 at the corresponding temperatures).

The domain size of anatase-type (100) surface terminations may thus affect the stability of the solid nanoparticle, but no clear correlation can be established with the kinetic parameters of the crystallization process displayed in Table 2. The activation energy (E_A) values were obtained from Arrhenius plots using the k rate constant of eq 1 and measured at three different temperatures. Figure 7 displays the (Raman) experimental data and linear fittings allowing to obtain it for the TA sample. For comparison, we may mention that values of 150−200 kJ mol^{-1} have been obtained previously for the E_A parameter in high surface area anatase-TiO_2 samples.[24] Kinetic differences among the anatase phase crystallization and growth samples, as described by the activation energy of the crystallization mechanism (E_A), seem thus a factor of several, combined physicochemical, surface-related variables, not easily discernible even with the combined XRD/Raman/IR approach used here. On the other hand, the strong E_A variation observed in our sample series contrasts with the moderate one (lower than 60 kJ mol^{-1}) measured for rutile nucleation and growth.[49] This fact suggests than anatase and rutile nucleation and growth processes do not share the same kinetic size dependence, as already addressed by Ghost et al.[23] As a final point, we can mention that this nucleation-dominated crystallization process leads to a T particle with elongated shape, showing (101) and (100) surface terminations, while TA and TB have more spherical shapes, having a more even development of (101), (100), and (001) terminations with higher spatial isotropy.[46−48] A larger number of the latter type of face would suggest that TB has in turn a larger degree of spatial isotropy than TA. Such shape differences imply, according to Barnard and Curtiss,[50] a different surface chemistry (OH density and net surface charge) and, moreover, a different anatase to rutile characteristic transformation size. The latter will be discussed below.

In conjunction with the nature and activation energies of the crystallization mechanism discussed above, it is quite interesting to explore the dynamics of grain growth in the nanoparticulated materials. It is well-known that nanoscale crystallites in oxide materials coarsen to large average grain sizes upon thermal treatments. Six different phenomena are believed to contribute toward the sintering of microsized particles: (i) surface diffusion, (ii) lattice diffusion from surface, (iii) vapor transport, (iv) grain boundary diffusion, (v) lattice diffusion from grain boundary, and (vi) lattice diffusion through dislocations.[40] However, the growth of anatase nanoparticles seems to be affected by many different parameters, including grain size of the particles prior to sintering, presence of solute or impurity species, hydration of surface layers, concentration of dislocation density at boundaries, and the presence of pores.[23−26,51,52] The influence of such effects is customarily studied by modeling the grain growth with an empirical rate law:

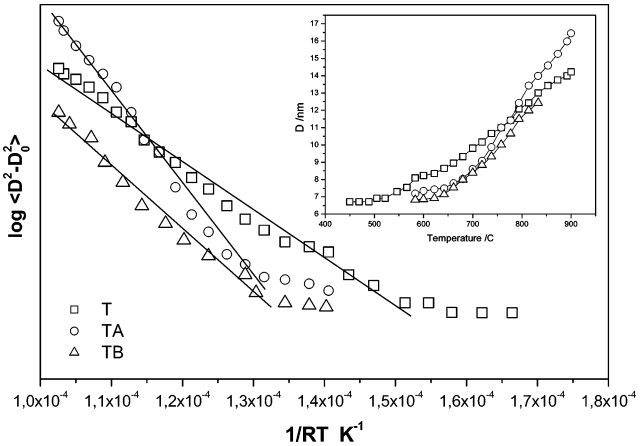

Figure 8. Arrhenius-type plot showing the temperature dependence of the anatase primary particle size growth as measured using XRD data. Inset: anatase primary particle size as a function of the treatment temperature under dry air.

$$D^m - D_0^m = kt \qquad (2)$$

where D is the instantaneous grain size, D_0 is the initial grain size, and m is the grain growth exponent.[25,53] D values were calculated here using Debye−Scherrer and Willianson−Hall formalisms, and no significant differences were encountered in the kinetic parameters reported in Table 2; this is probably because the main differences between D values obtained with these two methods can be encountered in the initial region after the nucleation onset due to the large line width of the XRD peaks. Figure 8 shows, however, that in a ca. 100 °C interval after the nucleation onset there is a rather slow growth of the line width without appreciable differences among our three samples. Normal grain growth in a pure, single phase should yield $m = 2$; this is in fact our case and also the case of systems with high initial purity.[25] As deduced from Figure 8, this gives activation energies in the 15−30 kJ mol^{-1} interval, roughly compatible with proton-transfer processes in forming ionized molecules.[25,54] This would mean that the hydration of surface and near-surface layers (e.g., the nature (acid/basic) and number of OH species) is a critical parameter to control growth size. This has been previously shown by Li et al.[25] and may be considered as an extension of the Barnard proposal that the surface chemistry (terminations) may affect phase transitions,[50] as here we are able to show that it affects growth behavior and, consequently, phase transition onset. Differences among our samples may be interpreted according to the data presented in Figures 6 and 9, which provide evidence of the presence of water precursor entities (interacting OH groups in Figure 6) evolving at higher temperature for the TA sample with respect to the T and TB samples (peak at ca. 350 °C in Figure 9). This would mean that the easier the water evolution throughout the thermal treatment, the lower the activation energy of the growth

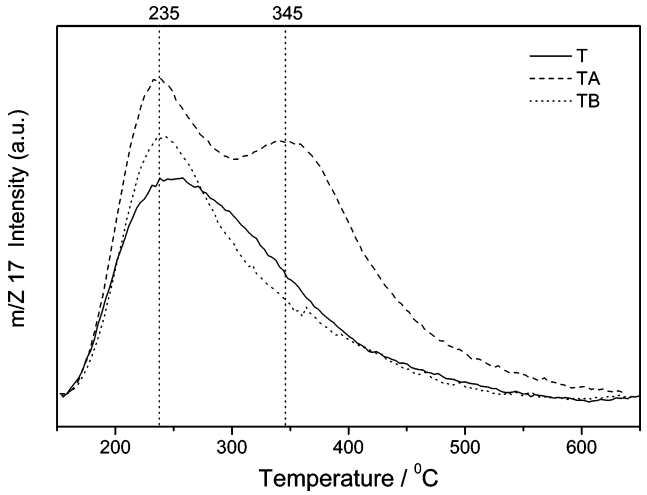

Figure 9. *M*/*z* 17 mass signal behavior during thermal treatment in dry air.

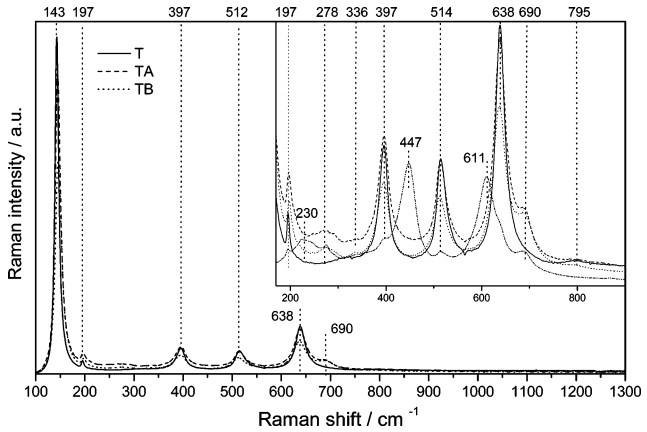

Figure 10. Raman spectra of Ti−O samples at room temperature after treatment at 900 °C under dry air. Inset: Detail showing bands (two spectra are displayed for TA corresponding to two different geometrical areas of the sample).

process and, consequently, the easier the control of the size. In our case, this occurs for the elongated-shape T sample.

Phase Behavior at High Temperature. XRD (Figure 4A) showed the presence of additional, minor phases in the TA samples above ca. 650 °C. Raman spectra recorded at room temperature of the systems treated at 900 °C (see Figure 10) provide additional evidence of the presence of a minor phase with characteristic frequencies at ca. 280 and 690 cm^{-1} in the TA and TB materials. Such phase does not correspond to any of the known polymorphs of TiO_2 (brookite, TiO_2(H), TiO_2-(R), and TiO_2(B)) usually detected with anatase and likely possesses a nearly cubic symmetry. According to the XRD plot (Figure 4A), such a phase does not grow from anatase and is stable in the whole temperature range scanned. In contrast, no other phase than anatase is detected by XRD/Raman in the case of the T sample. This sets a detection limit of less than 0.5 wt % for the presence of "impurity phases" in the later solid (assuming the detection limit of brookite—the only known minor phase stable at high temperature—using the more sensitive Raman spectroscopy).[55] The presence of this "impurity" may affect the crystallization mechanism; however, as can be seen in Table 2, the kinetic parameters do not allow differentiation between the T and TA/TB samples, giving support to the idea that the impurity is not critically affecting the reported results.

Similarly, the presence of rutile above 750 °C is only detected in the TA case (Figures 4 and 10). Rutile appears unhomogeneously distributed through the TA sample; Raman shows presence of both rutile and anatase rich zones (Figure 10, inset), depending on the progression degree of the anatase → rutile phase transformation, presumably as a function of the particle size of the individual anatase nanoparticles involved in such a transition. Detection of rutile only in the TA case further showed that the presence of a minor phase may not serve as potential nucleation sites for rutile nucleation, as has been previously proposed.[18] Such behavior would on the other hand indicate that the surface chemistry of the anatase nanoparticles may in fact play a key role in the phase transformation onset temperature, as mentioned above. In our studies, rutile appearance is blocked below 900 °C in the case of T and TB samples, suggesting that such an effect would have a rather complex structural basis. This will be the subject of future work where the structural basis of the phase behavior will be examined by using the atomic pair distribution function (PDF).[56]

Conclusions

This article analyzed nanoparticulated TiO_2 materials with anatase structure synthesized using a microemulsion method. Three different syntheses with varying surfactant-to-water molar ratio (ω) were used to obtain amorphous solid precipitates at room temperature. The adequate election of the synthesis parameters allows one to get a sample with anatase structure without the presence of minor impurity phases, stable up to 900 °C and with a size between ca. 7−20 nm as a function of the calcination temperature. More importantly, the particle size of the anatase nanoparticles can be carefully controlled within our experimental conditions. The grain growth kinetic analysis gives evidence that the hydration of surface layers (e.g., the surface OH-containing species nature and thermal stability/evolution) is a key parameter controlling size and maintaining the fine dimension of the nanoparticles obtained after the nucleation step. The corresponding activation energy values are low, indicating a weak temperature dependence of the growth process, which can be minimized upon our synthesis method using the T sample procedure.

The crystallization of the anatase structure in our samples does not follow a traditional nucleation and growth mechanism; the analysis using the Avrami formalism gives conclusive evidence of a surface nucleation-dominated process. Size of anatase nanomaterials is therefore dominated by this step, with grain growth being of much lesser importance. This behavior appears as a distinctive feature of anatase-TiO_2 nanomaterials, far from the corresponding behavior of microsized or bulk materials. Overall, our results show that the shape (i.e., elongated or isotropic), size (in the nanometer range), and surface nature and properties (OH nature and thermal properties; surface net charge) are strongly linked variables that control the two important physical phenomena: nucleation onset (temperature) and particle growth kinetics. It may be necessary to develop models that account for the interdependence of all three of these variables to correctly interpret phase and morphological behavior of anatase-TiO_2 samples.

Acknowledgment. The research carried out at the Chemistry Department of BNL was financed through Contract DE-AC02-98CH10886 with the U.S. Department of Energy (Division of Chemical Sciences). The NSLS is supported by the Divisions of Materials and Chemical Sciences of DOE. Work at the Instituto de Catálisis y Petroleoquímica (CSIC) was done with financial support from CICYT (Project CT2004-03409/BQU). We thank Dr. M. Bañares for the use of the Raman spectrometer.

C.B. thanks the Spanish Ministerio de Educación y Ciencia for a contract from the Juan de la Cierva program.

References and Notes

(1) Bosh, H.; Janssen, F. *Catal. Today* **1988**, *2*, 369.
(2) Forzatti, P. *Catal. Today* **2000**, *62*, 51.
(3) Hoffman, M. R.; Martin, S. T.; Choi, W.; Bahneman, D. W. *Chem. Rev.* **1995**, *95*, 69.
(4) Maldoti, A.; Molinari, A.; Amadeni, R. *Chem. Rev.* **2002**, *102*, 3811.
(5) Johnson, R. W.; Thieles, E. S.; French, R. H. *Tappi J.* **1997**, *80*, 233.
(6) Kalyanasendevan, K.; Gratzel, M. In *Optoelectronic Properties of Inorganic Compounds*; Roundhill, D. M., Fackler, J. P., Jr., Eds.; Plenum Press: New York, 1999; pp 169−194.
(7) *Gas Sensors*; Sheveglieri, G., Ed.; Kluwer: Dordrecht, The Netherlands, 1992.
(8) Phillips, L. G.; Barbeno, D. M. *J. Dairy Sci.* **1997**, *80*, 2726.
(9) Selhofer, H. *Vacuum Thin Films*, August, 1999, p 15.
(10) Fujishima, A.; Rao, T. N.; Tryk, D. A. *J. Photochem. Photobiol., C* **2000**, *1*, 1.
(11) Bonhole, P.; Gogniat, E.; Gratzel, M.; Ashrit, P. V. *Thin Solid Films* **1999**, *350*, 269.
(12) Fernández-García, M.; Martínez-Arias, A.; Hanson, J. C.; Rodriguez, J. A. *Chem. Rev.* **2004**, *104*, 4063.
(13) Marchand, R.; Broham, L.; Tournoux, M. *Mater. Res. Bull.* **1980**, *15*, 1129.
(14) Akimoto, J.; Gotoh, Y.; Oosawa, N.; Nonose, N.; Kumagai, T.; Aoki, K.; Takei, H. *J. Solid State Chem.* **1994**, *113*, 27.
(15) Latroche, M.; Brohan, L.; Marchand, R.; Tournoux, M. *J. Solid State Chem.* **1989**, *81*, 78.
(16) Muscat, J.; Swany, V.; Harrison, N. M. *Phys. Rev. B* **2002**, *65*, 224112.
(17) Zhang, H.; Bandfield, J. F. *J. Mater. Chem.* **1998**, *8*, 2073.
(18) Hu, Y.; Tsai, H. L.; Hung, C. L. *Mater. Sci. Eng., A* **2003**, *344*, 209.
(19) Cushing, B. L.; Kolesnichenko, V. L.; O'Connor, C. J. *Chem. Rev.* **2004**, *104*, 3893.
(20) Uskokovic, V.; Drofenik, M. *Surf. Rev. Lett.* **2005**, *12*, 239.
(21) Li, G.; Li, L.; Boerio-Goates, J.; Woodfield, B. F. *J. Mater. Res.* **2003**, *18*, 2664.
(22) Kutty, T. R. N.; Vivekanandran, R.; Murugaraj, P. *Mater. Chem. Phys.* **1998**, *19*, 533.
(23) Ghost, T. B.; Dhabal, S.; Datta, A. K. *J. Appl. Phys.* **2003**, *94*, 4577.
(24) Kirsch, B. L.; Richman, E. K.; Riley, A. E.; Tolbert, S. H. *J. Phys. Chem. B* **2004**, *108*, 12698.
(25) Li, G.; Li, L.; Boerio-Goates, J.; Woodfield, B. F. *J. Am. Chem. Soc.* **2005**, *127*, 8659.
(26) Koparde, V. N.; Cummings, P. T. *J. Phys. Chem. B* **2005**, *109*, 24280.
(27) Fuerte, A.; Hernández-Alonso, M. D.; Maira, A. J.; Martínez-Arias, A.; Fernández-García, M.; Conesa, J. C.; Soria, J.; Munuera, G. *J. Catal.* **2002**, *212*, 1.
(28) Klementev, K. V. *J. Phys. D: Appl. Phys.* **2001**, *34*, 209.
(29) Rodriguez, J. A.; Hanson, J. C.; Kim, J.-Y.; Liu, G.; Iglesias-Juez, A.; Fernández-García, M. *J. Phys. Chem. B* **2003**, *107*, 3535.
(30) (a) Norby, P.; Hanson, J. *Catal. Today* **1998**, *39*, 301 and references therein. (b) Chupas, P. J.; Ciraolo, M. F.; Hanson, J. C.; Grey, C. P. *J. Am. Chem. Soc.* **2001**, *123*, 1694.
(31) Hammersely, A. P.; Svensson, S. O.; Thompson, A. *Nucl. Instrum. Methods Phys. Res.* **1994**, *346*, 321.
(32) Snyder, R. L.; Fiala, J.; Bunge, H. J. *Defect and Microstructure Analysis by Diffraction*; Oxford University Press: New York, 1999.
(33) Farges, F.; Brown, G. E., Jr.; Rehr, J. J. *Phys. Rev. B* **1997**, *56*, 1809.
(34) Luca, V.; Djajanti, S.; Howe, R. F. *J. Phys. Chem. B* **1998**, *102*, 10650.
(35) Pertipino, C.; Solari, P. L.; Lamberti, C. *J. Phys. Chem. B* **2005**, *109*, 13132.
(36) Wu, Z. Y.; Ouvard, G.; Gressier, P.; Natoli, C. R. *Phys. Rev. B* **1997**, *55*, 10382.
(37) Iida, Y.; Furukawa, M.; Kato, K.; Morikawa, H. *Appl. Spectrosc.* **1997**, *51*, 673.
(38) Hsu, L. S.; Rujkorakarn, R.; Sites, J. R.; She, Y. *J. Appl. Phys.* **1986**, *59*, 3475.
(39) Lee, M. S.; Park, S. S.; Lee, G.-D.; Ju, C.-S.; Hong, S.-S. *Catal. Today* **2005**, *101*, 283.
(40) Zeng, P.; Zajac, S.; Clapp, P. C. *Mater. Sci. Eng., A* **1998**, *252*, 301.
(41) Zhu, H. L.; Averback, R. S. *Mater. Sci. Eng., A* **1995**, *73*, 27.
(42) Raut, J. S.; Bhagat, R. B.; Fichthorn, K. A. *Nanostruct. Mater.* **1998**, *10*, 837.
(43) Avrami, M. *J. Chem. Phys.* **1939**, *7*, 1102; **1941**, *9*, 177.
(44) Matsuita, K.; Sakka, S. *J. Non-Cryst. Solids* **1980**, *38*, 741.
(45) Exarhos, G. J.; Aloi, M. *Thin Solid Films* **1990**, *193*, 42.
(46) Dzwigaj, S.; Arrouvel, C.; Breysse, M.; Geantet, C.; Inoue, S.; Toulhoat, H.; Raybaud, P. *J. Catal.* **2005**, *236*, 245.
(47) Digne, M.; Sautet, P.; Breysse, M.; Touthoat, H. *J. Catal.* **2002**, *211*, 1.
(48) Digne, M.; Sautet, P.; Raybaud, P.; Euzen, P.; Touthoat, H. *J. Catal.* **2004**, *226*, 54.
(49) Zhang, A. H.; Banfield, J. F. *Chem. Mater.* **2005**, *17*, 3421.
(50) Barnard, A. S.; Curtiss, L. A. *Nano Lett.* **2005**, *5*, 1261.
(51) Ciesla, U.; Schacht, S.; Stucky, G. D.; Unger, K. K.; Schuth, F. *Angew. Chem., Int. Ed.* **1996**, *35*, 541.
(52) Tian, Z. R.; Tong, W.; Wang, J.-Y.; Duan, N.-G.; Drishnan, V. K.; Suib, S. L. *Science* **1997**, *276*, 926.
(53) Mayo, M. *Int. Mater. Rev.* **1996**, *41*, 85.
(54) Collier, W. B.; Ritzhaupt, G.; Devlin, J. P. *J. Phys. Chem.* **1984**, *88*, 363.
(55) Murad, E.; Koster, H. M. *Clay Miner.* **1999**, *34*, 479.
(56) Hanson, J. C.; Rodriguez, J. A.; Belver, C.; Fernández-García, M. Brookhaven National Laboratory, Upton New York, and Instituto de Catálisis y Petroleoquímica, CSIC, Madrid, Spain; unpublished results, 2006.